



SUBJECT AREAS:

NANOMEDICINE

INORGANIC CHEMISTRY

BIOMATERIALS

CANCER IMAGING

Received
20 August 2012Accepted
15 April 2013Published
29 April 2013

Correspondence and
requests for materials
should be addressed to
W.B.B. (wbbu@mail.
sic.ac.cn) or J.L.S.
(jlshi@sunm.shcnc.ac.
cn)

Computed tomography imaging-guided radiotherapy by targeting upconversion nanocubes with significant imaging and radiosensitization enhancements

Huaiyong Xing¹, Xiangpeng Zheng², Qingguo Ren², Wenbo Bu¹, Weiqiang Ge², Qingfeng Xiao¹, Shengjian Zhang³, Chenyang Wei¹, Haiyun Qu¹, Zheng Wang¹, Yanqing Hua², Liangping Zhou³, Weijun Peng³, Kuaile Zhao³ & Jianlin Shi¹

¹State Key Laboratory of High performance Ceramics and Superfine Microstructures, Shanghai Institute of Ceramics, Chinese Academy of Sciences, Shanghai, 200050, China, ²Department of radiation oncology, Shanghai Huadong Hospital, Fudan University, Shanghai, 200040, China, ³Department of radiology, Shanghai Cancer Hospital, Fudan University, Shanghai, 200032, China.

The clinical potentials of radiotherapy could not be achieved completely because of the inaccurate positioning and inherent radioresistance of tumours. In this study, a novel active-targeting upconversion theranostic agent (arginine-glycine-aspartic acid-labelled BaYbF₅: 2% Er³⁺ nanocube) was developed for the first time to address these clinical demands. Heavy metal-based nanocubes (~10 nm) are potential theranostic agents with bifunctional features: computed tomography (CT) contrast agents for targeted tumour imaging and irradiation dose enhancers in tumours during radiotherapy. Remarkably, they showed low toxicity and excellent performance in active-targeting CT imaging and CT imaging-guided radiosensitizing therapy, which could greatly concentrate and enlarge the irradiation dose deposition in tumours to enhance therapeutic efficacy and minimize the damage to surrounding tissues.

Radiotherapy can non-invasively generate toxic photoelectrons and radical species that can kill cancerous cells by delivering therapeutic X-rays to tumour regions without surgical risks and complications or without the systematic toxicity of chemotherapy. Despite these advantages, the clinical potentials of radiotherapy could not be realized completely until two critical radiotherapy-related challenges could be overcome. Firstly, the inaccuracy in tumour localization at pre- and intra-treatments could lead to inadequate dose coverage to the tumour target and overexposure to surrounding normal tissues, resulting in the failure of tumour control and occurrence of radiation-induced toxicity^{1–3}. Secondly, inherent radioresistance of tumours due to various mechanisms (such as hypoxia) needs high irradiation dose or anticancer drugs for effective eradication of cancerous cells^{4–6}.

Metal-based (usually silver or gold) fiducials are usually implanted into tumours or tumour beds to position the tumours for radiotherapy guidance, causing potential risks to patients. Interestingly, X-ray computed tomography (CT) could provide high-resolution three-dimensional (3D) structural details of tissues without any invasion, which is highly beneficial for radiotherapy location^{7,8}. Due to ionizing character of the X-ray beam, CT imaging is less safe than magnetic resonance imaging (MRI). However CT imaging guidance in radiotherapy has been the dominant imaging modality over MRI due to the following reasons: first, fast acquisition which makes the patient-on-treatment-couch time as short as possible; second, high reproducibility which allows continued comparison and evaluation of tumor positions at different treatment fractions. Third, CT imaging during treatment could be used to compare with planning CT imaging such as IGRT and TOMO radiotherapy in hospital. Given that the recognition of lesions in CT relies largely on their differential X-ray absorption features from the surroundings, contrast agents (CAs) are necessary to enhance these differences. Clinical CT CAs (iodine-based compounds) could detect tumours in a few seconds. However, these CAs suffer from very short circulation duration of the molecule iodinate *in vivo* (within a few minutes)^{9–11}. Newly developed nanoparticles (NPs) could be ideal candidates for a more efficient CT imaging to locate tumours because of their prolonged



circulation time, selective accumulation in tumours by the enhanced permeability and retention (EPR) effect^{12,13} and the promising active-targeting through conjugating special antibody or peptide¹⁰. Several metal (Au, Bi, Ta, Gd, Lu, *etc.*)-based NPs were synthesized as new CT CAs because of their high performance in X-ray attenuation (high Z) and stability *in vivo*^{14–21}. Interestingly, ytterbium (Yb)-based NPs with good biocompatibility were reported to possess higher attenuation than previously reported CAs, especially at a clinical 120 kVp scanner^{22,23}. The higher the attenuation that metal-based CAs have per unit, the lesser dosage would be required to achieve equal signal enhancement and high targeting efficiency for tumour imaging. Recently, Qu *et al.* have reported on the potential of Er³⁺-doped Yb₂O₃ NPs as efficient CT imaging CAs. However, they only focused on hepatic imaging with NPs captured by phagocytic cells in the reticuloendothelial system²⁴. Studies on active-targeted CT imaging based on Yb NPs for accurate tumour positioning are lacking.

Meanwhile, the problem of radioresistance is of equal importance in tumour control because of the extensive presence of radioresistant (*e.g.*, hypoxic, S-phase) tumour cells^{4,6}. In this aspect, the combination of chemotherapy and radiotherapy is a well-established strategy²⁵, but concerns on the overall toxicity have significantly retarded its adoption among many cancers^{26–28}. Another effective strategy in enhancing the localized irradiation dose in tumours is radiosensitization^{1,4,5}. Fortunately, heavy metal (with high Z) NPs as promising CT CAs could be used in radiosensitizing therapy because of their high X-ray photon capture cross-section and Compton scattering effect^{5,29,30}. Therefore, the X-ray dose of the surrounding tissue could be greatly reduced, and higher dose could be concentrated at the tumour region containing NPs. To date, gold (Au) NPs have been extensively investigated for their dose-enhancement effect. Au has K-edge at approximately 81 keV; irradiation using photon beams with energy in the keV range (*e.g.*, 200 keV) could induce dramatic emission of photoelectrons that damage biological macromolecules^{1,4,5}. Douglass developed a randomized 3D cell model for Monte Carlo microdosimetry simulations in the keV range³¹. McMahon showed the calculations of biological consequences of energy deposition near irradiated heavy atom NPs; the results of these calculations were consistent with cellular experiments under keV radiation²⁹. Hainfeld focused on radiotherapy enhanced with Au NPs *in vivo* but was only confined to low energy (kV) beam irradiation^{4,5,32}. Unfortunately, the clinical radiotherapy machines apply electron linacs with much higher energy (6 MV to 25 MV) that are much more penetrable to tissues than low energy (kV) beams, leading to less irradiation deposition in the skin³³. Notably, studies focusing on the effect of heavy metal NPs on the dose distribution of megavoltage (MV) irradiation would be more clinically relevant. However, such studies have been reported basically established on Monte Carlo modelling calculations or at the cellular level^{34–39}. Therefore, the radiosensitizing effect of MV irradiation *in vivo* is an interesting topic.

This study reports on the upconversion of BaYbF₅: 2% Er³⁺ nanocubes (UCA) conjugated with arginine-glycine-aspartic acid (RGD) peptides (UCA-RGD) as effective tumour-targeting theranostic agents with dual functions: efficient targeted CT CAs for tumour imaging and irradiation dose amplifier for radiotherapy under the guidance of CT imaging. This specifically designed dual metal element-based nanocube probe holds a great promise as CT imaging CA with better CT imaging quality at reduced CA dosage when compared with the current available CAs imaged using a clinical CT scanner. Meanwhile, compared with the conventional organic dyes or quantum dots, these upconversion NPs could be excited by near-infrared (NIR) laser and emit upconversion luminescence (UCL) with greatly suppressed autofluorescence, photodamage and toxicity, which could be ideal for cell or even tissue tracking^{40–42}. RGD peptides were selected for tumour-targeted imaging because of their

high binding affinities to $\alpha_v\beta_3$ integrin receptors overexpressed on the surface of endothelial cells lining the neovasculatures in tumours⁴³. Guided by tumour-targeted CT imaging, the radiosensitizing effect of heavy CT CAs was investigated using a clinical megavoltage photon beam.

Results

Characterization of UCA-RGD. Hydrophobic BaYbF₅:2% Er³⁺ NPs were synthesized using a hydrothermal method. This method was selected because it is simpler, more productive and more user-friendly than previously used thermolysis at high temperatures^{23,44}. The low cost and high productivity would satisfy the heavy use of CT CAs. The as-prepared NPs were characterized by X-ray powder diffraction (XRD, Figure S1a), which showed the cubic phase patterns when compared with the standard PDF card of BaGdF₅: 24-0098. The average crystallite size of NPs was approximately 9.4 nm, as calculated from the Scherrer formula ($D = K\lambda/\beta\cos\theta$, calculation in Figure S1 caption). All component elements (Ba, Yb, F and Er) were found in the energy dispersive X-ray (EDX) spectrum (Figure S1b). As shown in the transmission electron microscope (TEM) and scanning transmission electron microscope (STEM) images (Figures 1a, 1b, S2 and S3), the constructed oleic acid (OA)-coated NPs have a unique cube shape and an average size of 9.9 nm. These findings are consistent with those calculated from the Scherrer formula.

Biomimetic DSPE-PEG₂₀₀₀ and DSPE-PEG₂₀₀₀-Mal were used to endow the OA-BaYbF₅:2% Er³⁺ nanocubes with good hydrophilicity and biocompatibility. Thiolated RGD peptides were then conjugated to DSPE-PEG₂₀₀₀-Mal through classic thiol-maleimide reaction to produce targeting UCA-RGD⁴⁵. Figures 1c and S4 show excellent dispersion of UCA-RGD in water without any visible aggregation, which was further demonstrated by the small and well-defined hydrated size of 22 nm (Figure S5a). The obtained nanocubes displayed a potential as CT CAs. As shown in Figures 1d and 1e, the contrast efficiency of UCA was approximately three times higher than that of clinical Iobitridol because of their high X-ray absorption coefficients (*e.g.*, at 100 keV: Ba, 2.2 cm² g⁻¹; Yb, 3.88 cm² g⁻¹; I, 1.94 cm² g⁻¹)⁴⁶.

Targeted imaging *in vitro*. With the conjugation of RGD peptides, the Zeta potential of the solution changed from −24.8 mV to −6.4 mV (Figure S5b and S5c), along with the weakened characteristic band of CH₂ (*e.g.*, stretching vibrations of the C–H) and the intensified characteristic band of RGD (*e.g.*, stretching vibrations of C=O in O=C–N) (Figure S6). Inductively coupled plasma atomic emission spectroscopy (ICP-AES) showed that the molar ratio of S (RGD) and Yb (UCA) in the obtained UCA-RGD NPs was approximately 1 : 2. To investigate the targeting efficiency of UCA-RGD *in vitro*, human glioblastoma U87MG cells with high $\alpha_v\beta_3$ integrin expression and human breast cancer MCF-7 cells with low $\alpha_v\beta_3$ integrin expression served as positive/negative controls^{47,48}. Figure 1g shows that more than 85.9% of the U87MG cells and 89.8% of the MCF-7 cells survived after incubation with a high concentration of UCA-RGD (800 μ g Yb/mL) for 24 h. Notably, the cell viability remained >78% even after 2 d of co-incubation with UCA-RGD NPs (800 μ g Yb/mL, Figure S7), indicating the low cytotoxicity of UCA-RGD *in vitro*. Given that the BaYbF₅: 2% Er³⁺ nanocubes could emit strong red luminescence under excitation at 980 nm laser (Figure S8), the specific uptake of UCA-RGD by high $\alpha_v\beta_3$ integrin expressed U87MG cells could be directly observed in the confocal microscopic images. As shown in Figure 2, minimal UCL was observed in U87MG and MCF-7 cells incubated with non-targeting UCA alone. A similar finding was obtained in MCF-7 cells incubated with RGD-targeted UCA (UCA-RGD). Remarkably, maximum luminescence was detected in U87MG cells incubated with UCA-RGD. The blocking experiment was

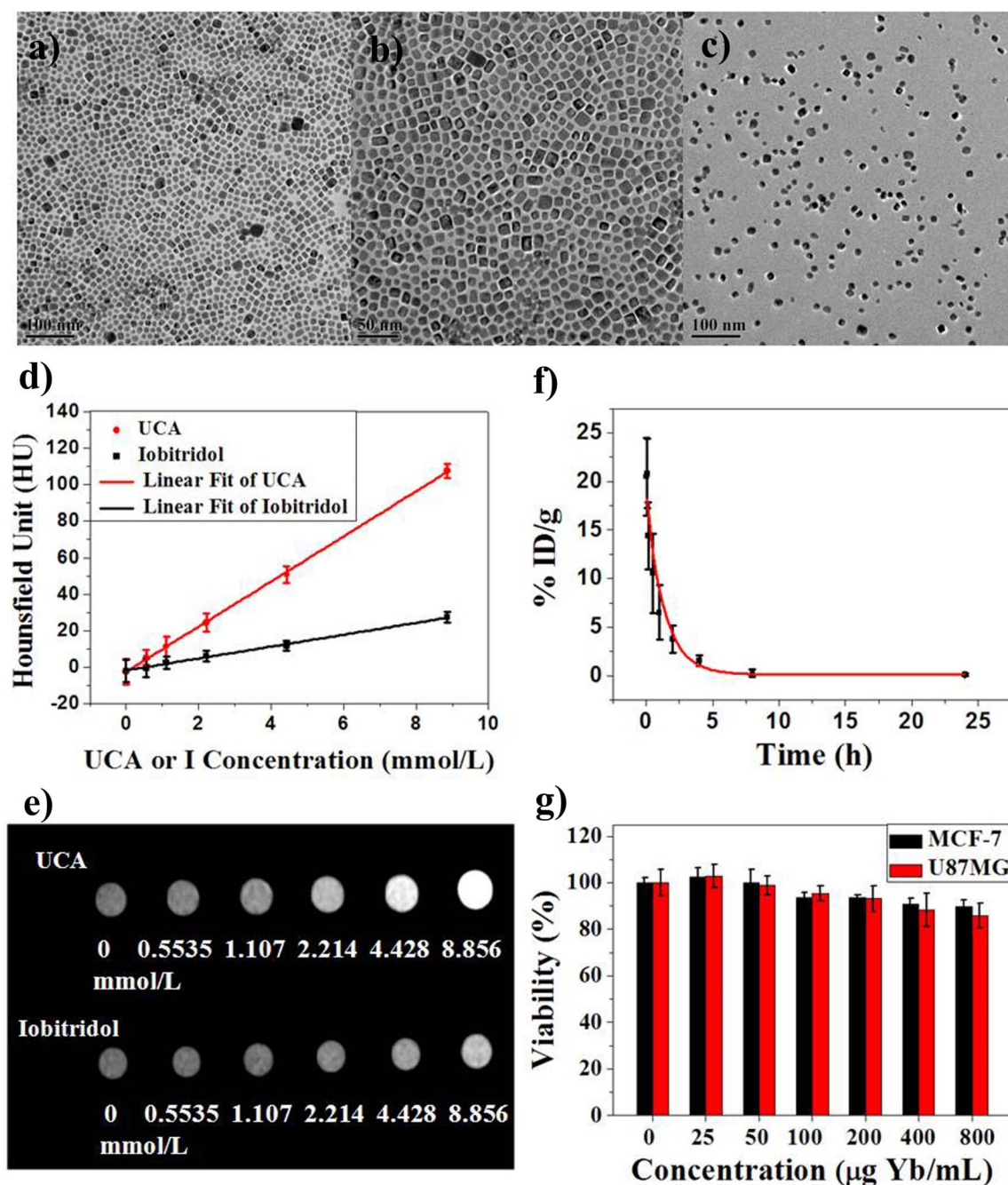


Figure 1 | (a, b) TEM images of OA-BaYbF₅:2% Er³⁺ nanocubes in chloroform; (c) TEM images of RGD-labelled UCA in water; (d) CT values and (e) images of UCA and Iobitridol with different concentrations; (f) *In vivo* blood terminal half-life (t_{1/2}) of UCA-RGD *in vivo* (n = 3) and (g) Cell viabilities of U87MG and MCF-7 cells incubated with UCA-RGD of different concentrations for 24 h.

performed using a large dose of pure RGD peptide (10 mg) for 1 h co-incubation, i.e., pre-treated U87MG cells were incubated with UCA-RGD NPs for another hour (Figure S9b). Much less NPs in the UCA-RGD group under high-dose RGD blocking were uptaken by U87MG cells when compared with the non-blocked group. Another control experiment was performed with UCA nanocubes functionalized by RAD [c(RAD)yC)] peptide through the classic thiol-maleimide reaction. In contrast to RGD, the peptides containing RAD exhibited low affinities to $\alpha_v\beta_3$ integrins^{49,50}. As shown in Figure S9c, minimal UCL was observed in U87MG cells incubated with UCA-RAD for 1 h, suggesting the insignificant non-specific cell uptake of UCA-RAD compared with the UCA-RGD after incubation. The cellular uptake of UCA and UCA-RGD NPs

by U87MG cells were also investigated in sectional TEM images after 1 h of co-incubation (Figure S10). Many UCA-RGD NPs were found localized at the cell surface or in the intracellular regions. However, only a negligible amount of UCA NPs were found in U87MG cells. This all indicates that the uptake in U87MG cells of nanoprobe is specifically enhanced by binding with RGD peptide.

Targeted imaging *in vivo*. To demonstrate the feasibility of active-targeting UCL imaging *in vivo*, Tm³⁺-doped UCA-RGD and UCA NPs that could emit strong NIR luminescence (approximately 800 nm, attributed to ³H₄ → ³H₆ of Tm³⁺ transition, Figure S11) under the same dosage (70 mg Yb/kg) were intravenously injected in U87MG tumour-bearing mice. The Tm³⁺-doped UCA-RGD and

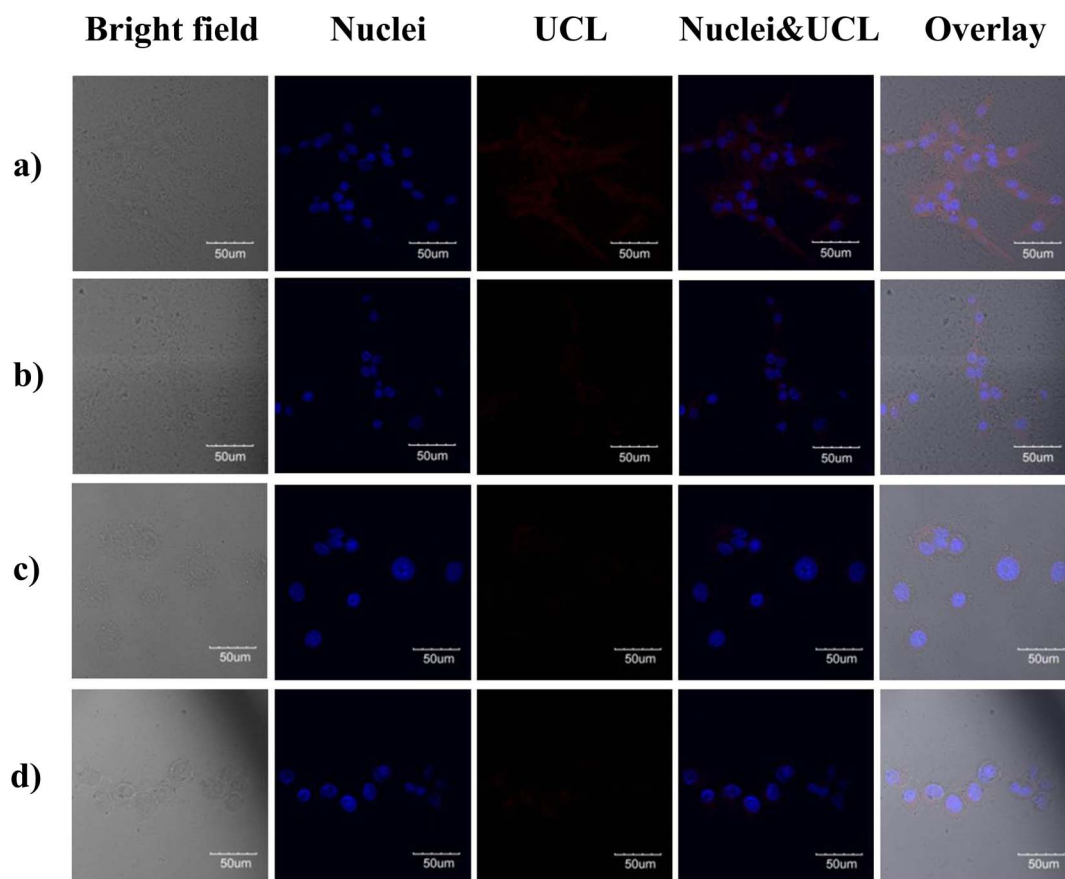


Figure 2 | Confocal UCL imaging of U87MG cells incubated with UCA-RGD (a) and UCA (b) at 800 μg Yb/mL for 1 h. UCL imaging of MCF-7 cells incubated with UCA-RGD (c) and UCA (d) at 800 μg Yb/mL for 1 h.

UCA NPs possess deeper tissue penetration because the NIR-to-NIR luminescence is in the ‘optical transmission window’ of tissues (750 nm to 1000 nm). Therefore, they are more suitable for *in vivo* imaging than Er^{3+} -doped NPs^{23,42,51}. After 3 h, the tumours of the targeted group (injected with UCA-RGD NPs) emitted significantly stronger luminescence than those of the non-targeted group (injected with UCA NPs) (Figure S12), indicating that more active-targeting UCA-RGD NPs were uptaken by the tumours than the non-targeting UCA NPs. Motivated by the exciting CT contrast performance and targeting efficiency in UCL modality, *in vivo* tumour-targeted CT imaging was performed using U87MG tumour-bearing mice by intravenous administration of the same dosage of UCA and UCA-RGD (70 mg Yb/kg). As shown in Figures 3a, S13 and S14, 3 hours after CA administration, the tumours from the targeted group could be readily recognized in CT images, especially through 3D volume rendering (VR) processing (marked in the yellow circle in Figure 3a, Movie S1), in contrast to the non-enhanced tumours from the non-targeted group (marked in the blue circle in Figure 3a, Movie S2). For quantitative analysis of the enhancement, the regions of interest (ROI) were localized in each tumour with fixed size and matching position. In the targeted group, the average Hounsfield unit (HU) value increased from 24.0 to 67.4 (** $p < 0.001$), as judged by clinical radiological criteria. However, in the non-targeted group, a mild HU enhancement of 17.5 (from 29.4 to 46.9, * $p < 0.05$) occurred because of the EPR effect. The tumour HU value enhancement in the targeted group was approximately 2.5-fold that in the non-targeted group (Figure 3b). For an accurate biodistribution determination of UCA-RGD or UCA in mice, the concentrations of Yb in each organ harvested immediately were measured after

imaging acquisition ($n = 3$) using ICP-AES (Figure 3c). Despite the extensive splenic and hepatic deposition, a considerable amount of UCA-RGD accumulated in tumours (approximately 7.5% ID Yb/g), which is 3.3-fold the UCA deposition in the non-targeted group (only approximately 2.3% ID Yb/g). This result is consistent with the observation in imaging enhancement. In addition, CT imaging was also recorded with UCA-RAD injection under the same condition with UCA-RGD injection (3 h after injection of UCA-RAD with 70 mg Yb/kg). As shown in Figure S15, although the tumour injected with UCA-RAD could be observed, it was less remarkable than the UCA-RGD-injected group from the 3D VR CT images (marked in the red circle). This result further demonstrates that the accumulation in tumours is due to the presence of RGD. Thus, UCA-RGD with high tumour selectivity and affinity could be used as an efficient tumour targeting CT CA *in vivo*. Histological examination of critical organs (heart, kidney, liver, lung and spleen) stained with haematoxylin and eosin (H&E) showed no abnormal microscopic tissue changes, indicative of the favourable biocompatibility of UCA *in vivo* (Figure S16). For further comparison, clinical CT CA-Iobitridol was used at fivefold concentration of UCA-RGD. Unfortunately, the tumour imaging contrasts were not significantly enhanced, and Iobitridol was rapidly excreted *via* the urinary route (Figures S17 and S18).

Radiosensitization assessment *in vitro*. The irradiation dose enhancement of UCA was evaluated by typical polymer gels with magnetic resonance properties that change once irradiated. As shown in Figure S19, the addition of UCA dramatically shortened the T_2 value of gels with grey appearance of lower signal after

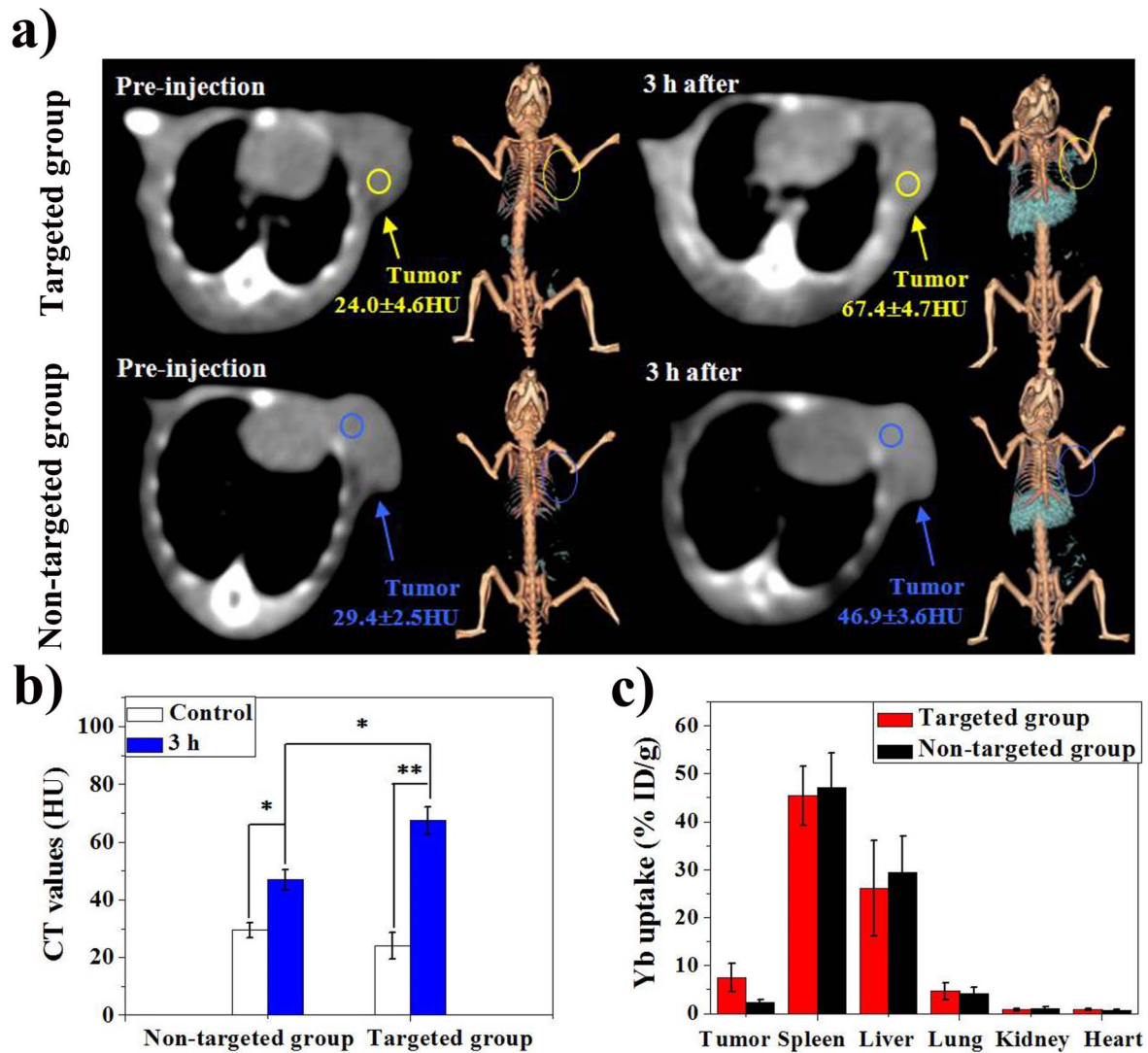


Figure 3 | (a) *In vivo* transverse slices and 3D volume rendering CT images of U87MG tumour-bearing mice at pre-injection and 3 h after intravenous injection of UCA-RGD (targeted group) or UCA (non-targeted group); the corresponding CT value changes in the tumour (b) and tissue distributions (n = 3) of NPs *in vivo* (c).

irradiation when compared with T₂-weighted images of gels without UCA. UCA could apparently increase irradiative energy deposition in gels, as reflected by magnetic resonance imaging (MRI).

Radiosensitization assessment *in vivo*. The findings of *in vitro* radiosensitization have encouraged us to perform translational *in vivo* experiments based on the U87MG tumour xenografts to investigate whether the dose enhancement effect could be applied to improve tumour control in radiotherapy. Notably, such radiotherapy could be guided well by CT imaging, as shown in Figure 3, wherein the radio-irradiation could be localized on the tumour site under on-line monitoring by CT imaging. The radiotherapy was conducted at 8 Gy radiation dose, 3 h after the intravenous injection of NPs. The treatment results are shown in Figure 4. The tumours in the control group without any treatment grew rapidly in the entire period of investigation, which enlarged nearly by 14-fold in tumour volume for 20 d. In the group treated with radiotherapy alone, tumour growth was inhibited only in the first 8 d, accompanied by an approximately 18% volume decrease. The UCA-injected radiation group showed similar tumour-inhibition behaviour with the radiotherapy-alone group because of the low UCA accumulation in the tumours (approximately 2.3% ID

Yb/g). By contrast, the tumours that received a combination of radiotherapy and UCA-RGD intravenous injection shrank by a maximum volume percentage of 35%, with growth inhibition that lasted for at least 12 d. The tumours regrew 14 d after radiotherapy. However, the UCA-RGD-assisted radiotherapy group regrew much slower than the other radiotherapy groups during the succeeding 8 d (**p < 0.001). Histopathological examination of dissected U87MG tumour tissues showed that the UCA-RGD alone had no therapeutic effect on the tumours. Compared with radiotherapy alone, UCA-RGD-assisted radiotherapy caused a more remarkable and extensive tissue destruction, such as large vacuoles and irregular widening (Figure S20).

Discussion

The contrast efficiency of UCA was approximately fourfold that of Iobitridol. Therefore, these efficient CT CAs could greatly reduce the usage of CAs, ensure the anatomical delineation with high quality and even benefit targeted tumour CT imaging. Through phospholipid-PEGylation, UCA-RGD acquired a long *in vivo* blood circulation half-life of up to 2.2 h (Figure 1f), which was much higher than the previously reported upconversion NPs (less than 10 min)⁵². A long circulation time benefits targeted imaging because targeting agents

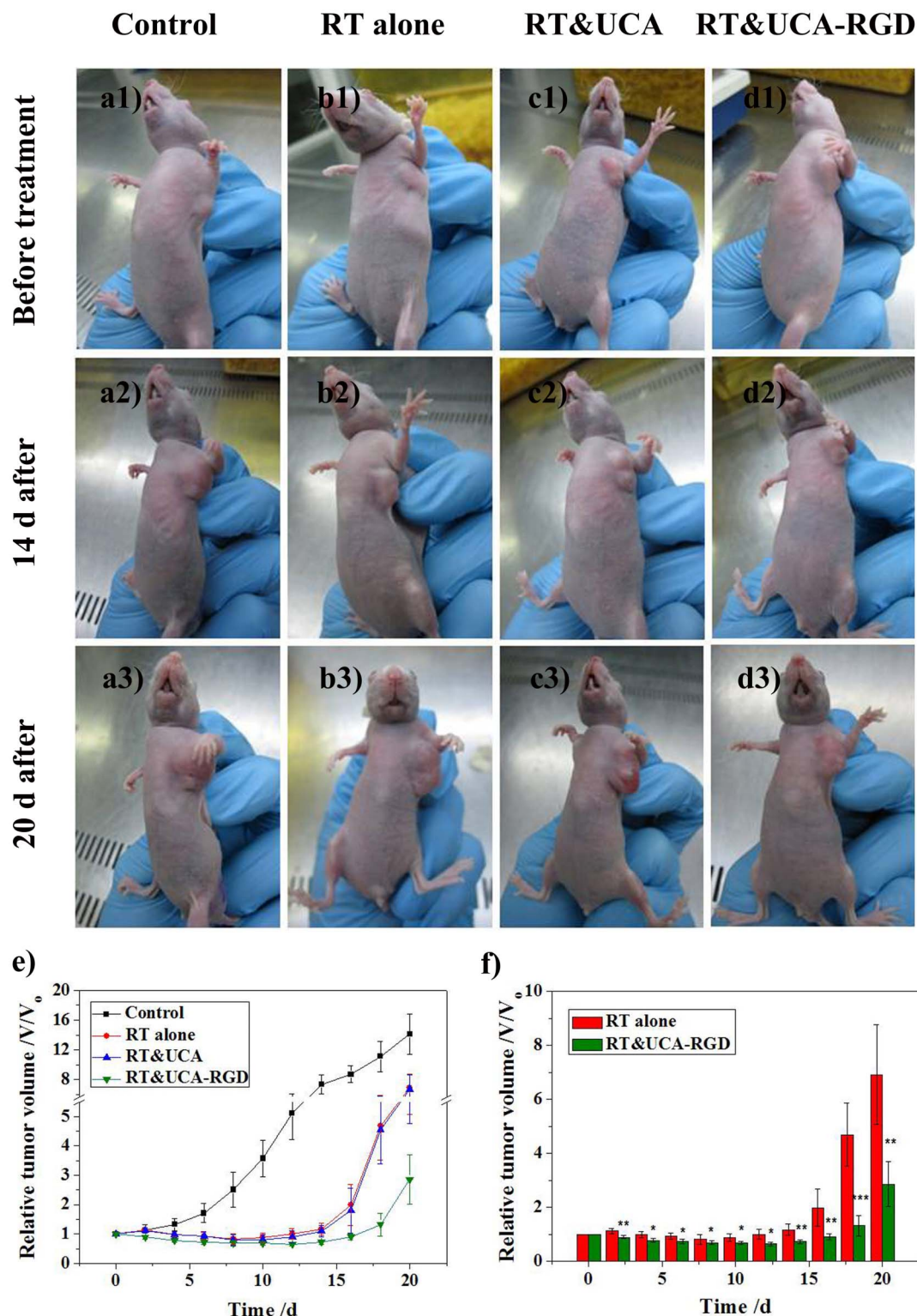


Figure 4 | Representative images of U87MG tumour-bearing mice at pre-injection 14 d and 20 d after various treatments: (a) Control without any treatment, (b) Radiotherapy alone, (c) Radiotherapy and UCA with intravenous injection of UCA (70 mg Yb/kg), (d) Radiotherapy and UCA-RGD with intravenous injection of UCA-RGD (70 mg Yb/kg). (e, f) Growth of U87MG tumours from different groups after various treatments ($n = 6$).

maintaining a relatively high blood concentration could be readily uptaken by target tissues. *In vivo* CT imaging shows that UCA-RGD with good biocompatibility can act as efficient CT CAs for active tumour targeting and imaging. Furthermore, the accurate diagnosis in CT modality using UCA-RGD could provide useful tools for the succeeding radiotherapy.

Theranosis combines diagnosis and simultaneous therapy. This concept, especially in imaging-guided therapy, has recently drawn extensive interests for future clinical applications^{3,53,54}. Effective theranosis relies largely on the efficient delivery of both imaging agents and drugs without separation before arriving at the tumour⁵⁵. Considering the designed theranosis system in the study, the targeted



UCA-RGD has shown active tumour-targeting capability compared with UCA alone. Moreover, CT CAs are effective 'drugs' that sensitize radiotherapy, without the need of carrying other additional drugs. In the present study, the heavy metal components in UCA could dramatically increase X-ray attenuation by inducing a cascade of photon-mass interaction along the pathway of incident photons. As a result, a large amount of photoelectrons and Auger electrons would be produced in tumours where UCA is accumulated³⁰. Given that RGD peptides have high binding affinities with $\alpha_v\beta_3$ integrin receptors, which are overexpressed in the new vasculature within U87MG tumours, a large amount of UCA-RGD could accumulate and distribute around the vascular endothelial lining (Figure S21)^{49,56}. During radiotherapy, tumour neovasculature was subjected to increased irradiation dose because of the dose enhancement effect by UCA-RGD, which could aggravate endothelial damage and vascular destruction, and the consequent blockade of nutrient delivery towards tumours^{4,35}. Additionally, less weight loss in mice treated with UCA-RGD-assisted radiotherapy than those in control group implied better physical condition and less tumour burden in mice (Figure S22). This result is consistent with better tumour control, which could be further translated as a better quality of life in the treatment of cancer patients.

In summary, we developed a novel active-targeting theranostic agent for targeted CT imaging and CT imaging-guided radiotherapy with a significant radiosensitization enhancement. Compared with the conventional CT CAs-enhanced imaging, the non-invasive targeted CT imaging could provide better anatomical and pathophysiological information of tumours for detection, treatment evaluation, target delineation and precise positioning for accurate CT imaging-guided radiotherapy of tumours. Furthermore, the constitutive heavy elements in this novel agent have been demonstrated capable of enhancing irradiation dose deposition by a radiosensitizing effect. The preliminary results from tumour xenografts showed that the dose enhancement effect observed *in vivo* could be readily translated to favourable tumour control by the UCA-RGD-radiosensitized radiotherapy. Meanwhile, the targeted theranostic system is anticipated to address the clinical drawbacks of radiotherapy through tumour positioning and sensitization, which could be used for the recognition and eradication of the whole tumour.

Methods

Synthesis of OA-BaYbF₅:2% Er³⁺ (Tm³⁺) nanocubes. The synthesis of BaYbF₅:2% Er³⁺ (Tm³⁺) nanocubes was conducted through a hydrothermal method following the procedures of previous studies with slight modification^{57,58}. In a typical procedure, ethanol (20 mL) was mixed with OA (12 mmol) and oleylamine (12 mmol) under magnetic stirring for 30 min to form a homogeneous solution. Subsequently, 1 mmol of BaCl₂ and RECl₃ (RE = 98% Yb³⁺, 2% Er³⁺ or Tm³⁺) solution (5 mL) was added into the previous solution. The solution was then slowly added with 5 mmol of NaF solution (5 mL). After stirring for 15 min, the mixture was transferred into a 100 mL Teflon-lined stainless steel autoclave, sealed and then kept at 160°C for 12 h. After being naturally cooled down to room temperature, the prepared samples were collected at the bottom of the vessel and then washed several times with chloroform and ethanol. Therefore, the OA-BaYbF₅:2% Er³⁺ nanocubes were obtained and redispersed in chloroform.

Synthesis of UCA. The as-prepared BaYbF₅:2% Er³⁺ (Tm³⁺) nanocubes were hydrophobic and could not be used in biological application. For good biocompatibility, DSPE-PEG₂₀₀₀ was used to modify the surface of hydrophobic nanocubes according to a previously reported method with slight modifications⁵⁹. Typically, 5 mL of BaYbF₅:2% Er³⁺ (Tm³⁺) solution in chloroform (20 mg/mL) was added into 5 mL DSPE-PEG₂₀₀₀ solution in chloroform (20 mg/mL) and then stirred for 10 min. The mixture was incubated at 60°C under vacuum in a rotary evaporator for 1 h to evaporate the solvent. Subsequently, 5 mL of physiological saline was added into the lipidic film and then sonicated for 5 min. The resulting solution was filtered through a 0.22 µm membrane filter to remove large aggregates and then kept at 4°C for later use.

Synthesis of UCA-RGD. First, maleimide-functionalized UCA-Mal micelles were prepared by mixing 5 mL of BaYbF₅:2% Er³⁺ (Tm³⁺) solution in chloroform (20 mg/mL), 4.5 mL DSPE-PEG₂₀₀₀ solution in chloroform (20 mg/mL) and 0.5 mL DSPE-PEG₂₀₀₀-Mal solution in chloroform (20 mg/mL). The mixture was stirred for 10 min and then incubated at 60°C under vacuum in a rotary evaporator for 1 h to

evaporate the solvent. Subsequently, 10 mL of water was added into the solid lipidic mass, and the solution was sonicated for 5 min. The thiolated RGD peptide-c(RGDyC) was conjugated with UCA-Mal micelles through specific thiol-maleimide crosslinking⁴⁵. Typically, 80 mg c(RGDyC) was added into the UCA-Mal solution and stirred for 24 h. The resulting solution was centrifuged three times to remove the residual RGD peptide and redispersed in 5 mL of physiological saline. The solution was filtered through a 0.22 µm membrane filter to remove large aggregates and then kept at 4°C for later use.

Synthesis of UCA-RAD. The synthesis process was relatively similar with UCA-RGD using c(RADyC) peptide rather than c(RGDyC).

Cell culture and cytotoxicity assessment. Human glioblastoma-astrocytoma U87MG cells were cultured at 37°C under 5% CO₂ in Dulbecco's Modified Eagle's Medium (DMEM) supplemented with 10% fetal bovine serum (FBS) and 1% penicillin/streptomycin. Human breast adenocarcinoma MCF-7 cells were cultured at 37°C under 5% CO₂ in Roswell Park Memorial Institute medium (RPMI) 1640 supplemented with 10% FBS and 1% penicillin/streptomycin. Both cells were purchased from Shanghai Institutes for Biological Sciences, China. The cytotoxicity assessment was measured by the typical 3-(4,5-dimethylthiazol-2-yl)-2,5-diphenyltetrazolium bromide (MTT) assay. U87MG and MCF-7 cells were seeded into a 96-well cell culture plate at 10⁴/well and then incubated for 24 h or 48 h at 37°C under 5% CO₂. DMEM/RPMI 1640 solutions of UCA-RGD with different concentrations of 25, 50, 100, 200, 400 and 800 µg Yb/mL were added to the wells. The cells were then incubated for 24 h at 37°C under 5% CO₂. The cell viabilities were calculated using the typical MTT assay.

Cellular confocal fluorescence imaging. Approximately 800 µg of Yb/mL UCA-RGD, UCA or UCA-RAD was incubated with U87MG or MCF-7 cell (10⁴/well) for 1 h at 37°C under 5% CO₂. After being washed thrice with PBS, the nuclei were stained with 1 µg/mL to 2 µg/mL 4'-6-diamidino-2-phenylindole (DAPI, λ_{ex} = 358 nm) for 15 min. Upconversion luminescent cellular imaging was acquired using an Olympus FV1000 laser-scanning microscope equipped with a CW NIR laser (λ_{ex} = 980 nm). A 60 × oil-immersion objective lens were used, and luminescence signals were observed in the wavelength region of 600 nm to 700 nm.

Measurement of blood terminal half-life *in vivo*. Specific-pathogen-free (SPF) healthy Kunming mice (~20 g, n = 3) were purchased and raised at the Laboratory Animal Centre, Shanghai Medical College of Fudan University, China. The mice were injected with 200 µL of UCA-RGD (7 mg Yb/mL, 70 mg Yb/kg) intravenously through the tail vein. All animal experiments were conducted under protocols approved by the Laboratory Animal Centre of Fudan University, China. The terminal half-life was measured by drawing approximately 15 µL of blood from the tail vein of the Kunming mice after injection (2 min, 5 min, 10 min, 0.5 h, 1 h, 2 h, 4 h, 8 h and 24 h). Each blood sample was dissolved in 1 mL of physiological saline (10 mmol/L EDTA, blood anticoagulant). The concentrations of UCA (Yb) in the blood were measured by ICP-AES. Terminal half-life was then calculated based on a single-component pharmacokinetic model.

***In vivo* CT imaging and biodistribution of UCA.** CT tests were performed on GE discovery CT750 HD, GE Healthcare, with spectral CT scanning mode and 0.625 mm slice thickness using the following parameters: detector coverage, 20.0 mm; pitch and speed, 0.531:1 and 10.62 mm; and gantry rotation time, 0.5 s. *In vivo* CT imaging of U87MG tumour-bearing mice was performed in various time periods after the intravenous injection of physiological saline with 200 µL of UCA-RGD (targeted group) or UCA (non-targeted group) with the same concentration (7 mg Yb/mL, 70 mg Yb/kg). At 3 h after the injection, the mice from the targeted group (n = 3) and the non-targeted group (n = 3) were sacrificed. The corresponding dissected organs were treated with microwave digestion. The biodistributions of UCA-RGD or UCA were then measured by the determination of Yb concentrations in the dissected organs using ICP-AES. Statistical analysis was performed using the Student's two-tailed t test (*p < 0.05, **p < 0.001, ***p < 0.0001).

Evaluation of radiosensitizing UCA *in vitro*. The evaluation of the radiosensitizing effect of UCA was performed on the polymer gels with magnetic resonance properties that changed when irradiated. Radiation-sensitive methacrylic and ascorbic acid in gelatin initiated by copper (MAGIC) gels were manufactured with slight modification⁶⁰. Gelatin (8 g) was added into 70 mL of water (50°C) under magnetic stirring for 30 min to form a homogeneous solution. Hydroquinone (200 mg) in 4.8 mL of water was added, and the solution was cooled down to 37°C. Subsequently, ascorbic acid (35.2 mg in 5 mL of water), CuSO₄·5H₂O (2 mg in 3 mL of water) and 9 g of methacrylic acid were added to the solution and stirred for 1 h. UCA (50 mg) was then added and stirred for another hour. The MAGIC gels were transferred in a refrigerator for storage overnight at approximately 18 h. After irradiation with 8 Gy dose, the gels were scanned using a Siemens 3.0-T Vero clinical MR scanner (repetition time: 8 s, echo delay time: 40 ms) for measuring radiation dose distributions in MAGIC gels.

Radiotherapy and treatment evaluation. Through the CT 3D-modeling auxiliary location, the radiotherapy was conducted at 8 Gy radiation dose, 3 h after the intravenous injection of NPs, on a Siemens Primus clinical linear accelerator (6 MeV) using a 1.5 cm × 3 cm radiation field to cover the entire tumour without the need of



critical anatomies at a source-to-skin distance (SSD) of 100 cm. The treatment evaluation of radiotherapy was performed from the pathological examinations of tumour tissues. The changes in tumour volumes and the whole body weights collected every other day were also noted. The tumour volumes were calculated using the equation $V = (\pi/6) \times L_{\max} \times W_{\max}^2$, where L_{\max} is the maximum tumour length of tumour and W_{\max} is the maximum tumour width. The relative tumour volumes were normalized to their initial sizes. Each group was conducted on sextuplet mice, wherein statistical analysis was performed using Student's two-tailed t test (* $p < 0.05$, ** $p < 0.001$, *** $p < 0.0001$).

- McMahon, S., Mendenhall, M., Jain, S. & Currell, F. Radiotherapy in the presence of contrast agents: a general figure of merit and its application to gold nanoparticles. *Phys. Med. Biol.* **53**, 5635–5651 (2008).
- Kobayashi, K., Usami, N., Porcel, E., Lacombe, S. & Le Sech, C. Enhancement of radiation effect by heavy elements. *Mutat. Res.-Rev. Mutat.* **704**, 123–131 (2010).
- Le Duc, G. *et al.* Toward an image-guided microbeam radiation therapy using gadolinium-based nanoparticles. *ACS Nano* **5**, 9566–9574 (2011).
- Hainfeld, J. F., Dilmanian, F. A., Slatkin, D. N. & Smilowitz, H. M. Radiotherapy enhancement with gold nanoparticles. *J. Pharm. Pharmacol.* **60**, 977–985 (2008).
- Hainfeld, J. F. *et al.* Gold nanoparticles enhance the radiation therapy of a murine squamous cell carcinoma. *Phys. Med. Biol.* **55**, 3045–3059 (2010).
- Suit, H. D. & Gerweck, L. E. Potential for hyperthermia and radiation therapy. *Cancer Res.* **39**, 2290–2298 (1979).
- Edholm, P. Computed tomography - new technique in diagnostic radiology. *P. Roy. Soc. B-Biol. Sci.* **195**, 277–279 (1977).
- Munzenrider, J. E., Pilepich, M., Reneferro, J. B., Tchakarova, I. & Carter, B. L. Use of body scanner in radiotherapy treatment planning. *Cancer* **40**, 170–179 (1977).
- Bourin, M., Joliet, P. & Ballereau, F. An overview of the clinical pharmacokinetics of X ray contrast media. *Clin. Pharmacokinet.* **32**, 180–193 (1997).
- Shilo, M., Reuveni, T., Motiei, M. & Popovtzer, R. Nanoparticles as computed tomography contrast agents: current status and future perspectives. *Nanomedicine-Uk* **7**, 257–269 (2012).
- Liu, Y., Ai, K. & Lu, L. Nanoparticulate X-ray computed tomography contrast agents: from design validation to *in vivo* applications. *Accounts Chem. Res.* **45**, 1817–1827 (2012).
- Maeda, H. The enhanced permeability and retention (EPR) effect in tumor vasculature: the key role of tumor-selective macromolecular drug targeting. *Adv. Enzyme Regul.* **41**, 189–207 (2001).
- Greish, K. Enhanced permeability and retention of macromolecular drugs in solid tumors: a royal gate for targeted anticancer nanomedicines. *J. Drug Target.* **15**, 457–464 (2007).
- Hainfeld, J. F., Slatkin, D. N., Focella, T. M. & Smilowitz, H. M. Gold nanoparticles: a new X-ray contrast agent. *Brit. J. Radiol.* **79**, 248–253 (2006).
- Rabin, O., Manuel Perez, J., Grimm, J., Wojtkiewicz, G. & Weissleder, R. An X-ray computed tomography imaging agent based on long-circulating bismuth sulphide nanoparticles. *Nat. Mater.* **5**, 118–122 (2006).
- Oh, M. H. *et al.* Large-scale synthesis of bioinert tantalum oxide nanoparticles for X-ray computed tomography imaging and bimodal image-guided sentinel lymph node mapping. *J. Am. Chem. Soc.* **133**, 5508–5515 (2011).
- He, M. *et al.* Dual phase-controlled synthesis of uniform lanthanide-doped NaGdF₄ upconversion nanocrystals via an OA/ionic liquid two-phase system for *in vivo* dual modality imaging. *Adv. Funct. Mater.* **21**, 4470–4477 (2011).
- Zhu, X. *et al.* Core-shell Fe₃O₄@NaLuF₄:Yb,Er/Tm nanostructure for MRI, CT and upconversion luminescence tri-modality imaging. *Biomaterials* **33**, 4618–4627 (2012).
- Hainfeld, J. F. *et al.* Micro-CT enables microlocalisation and quantification of Her2-targeted gold nanoparticles within tumour regions. *Brit. J. Radiol.* **84**, 526–533 (2011).
- Kinsella, J. M. *et al.* X-Ray computed tomography imaging of breast cancer by using targeted peptide-labeled bismuth sulfide nanoparticles. *Angew. Chem. Int. Ed.* **50**, 12308–12311 (2011).
- Xing, H. *et al.* Multifunctional nanoprobe for upconversion fluorescence, MR and CT trimodal imaging. *Biomaterials* **33**, 1079–1089 (2012).
- Liu, Y. *et al.* A high-performance ytterbium-based nanoparticulate contrast agent for *in vivo* X-ray computed tomography imaging. *Angew. Chem. Int. Ed.* **51**, 1437–1442 (2012).
- Xing, H. *et al.* A NaYbF₄:Tm³⁺ nanoprobe for CT and NIR-to-NIR fluorescent bimodal imaging. *Biomaterials* **33**, 5384–5393 (2012).
- Liu, Z. *et al.* Long-circulating Er³⁺-doped Yb₂O₃ up-conversion nanoparticle as an *in vivo* X-Ray CT imaging contrast agent. *Biomaterials* **33**, 6748–6757 (2012).
- Seiwert, T. Y., Salama, J. K. & Vokes, E. E. The chemoradiation paradigm in head and neck cancer. *Nat. Clin. Prac. Oncol.* **4**, 156–171 (2007).
- Boige, V. & Ducreux, M. Prevention and treatment of chemotherapy-induced digestive toxicities. *B. Cancer* **88**, 163–173 (2001).
- Forastiere, A. A. *et al.* Concurrent chemotherapy and radiotherapy for organ preservation in advanced laryngeal cancer. *New Engl. J. Med.* **349**, 2091–2098 (2003).
- Koo, H. *et al.* *In vivo* targeted delivery of nanoparticles for theranosis. *Accounts Chem. Res.* **44**, 1018–1028 (2011).
- McMahon, S. J. *et al.* Biological consequences of nanoscale energy deposition near irradiated heavy atom nanoparticles. *Sci. Rep.* **1**, 1–9 (2011).
- Das, I. J. & Kahn, F. M. Backscatter dose perturbation at high atomic number interfaces in megavoltage photon beams. *Med. Phys.* **16**, 367–375 (1989).
- Douglass, M., Bezak, E. & Penfold, S. Development of a randomized 3D cell model for Monte Carlo microdosimetry simulations. *Med. Phys.* **39**, 3509–3519 (2012).
- Hainfeld, J. F., Slatkin, D. N. & Smilowitz, H. M. The use of gold nanoparticles to enhance radiotherapy in mice. *Phys. Med. Biol.* **49**, 309–315 (2004).
- Berbeco, R. I. *et al.* DNA damage enhancement from gold nanoparticles for clinical MV photonbeams. *Radiat. Res.* **178**, 604–608 (2012).
- Rahman, W. N. *et al.* Enhancement of radiation effects by gold nanoparticles for superficial radiation therapy. *Nanomed-Nanotechnol.* **5**, 136–142 (2009).
- Berbeco, R. I., Ngwa, W. & Makrigiorgos, G. M. Localized dose enhancement to tumor blood vessel endothelial cells via megavoltage X-rays and targeted gold nanoparticles: new potential for external beam radiotherapy. *Int. J. Radiat. Oncol.* **81**, 270–276 (2011).
- Liu, C. J. *et al.* Enhancement of cell radiation sensitivity by pegylated gold nanoparticles. *Phys. Med. Biol.* **55**, 931–945 (2010).
- McMahon, S. J. *et al.* Nanodosimetric effects of gold nanoparticles in megavoltage radiation therapy. *Radiother. Oncol.* **100**, 412–416 (2011).
- Chithrani, D. B. *et al.* Gold nanoparticles as radiation sensitizers in cancer therapy. *Radiat. Res.* **173**, 719–728 (2010).
- Jain, S. *et al.* Cell-specific radiosensitization by gold nanoparticles at megavoltage radiation energies. *Int. J. Radiat. Oncol.* **79**, 531–539 (2011).
- Wang, F. *et al.* Simultaneous phase and size control of upconversion nanocrystals through lanthanide doping. *Nature* **463**, 1061–1065 (2010).
- Nam, S. H. *et al.* Long-term real-time tracking of lanthanide ion doped upconverting nanoparticles in living cells. *Angew. Chem. Int. Ed.* **50**, 6093–6097 (2011).
- Zhou, J., Liu, Z. & Li, F. Upconversion nanophosphors for small-animal imaging. *Chem. Soc. Rev.* **41**, 1323–1349 (2012).
- Cai, W. & Chen, X. Multimodality molecular imaging of tumor angiogenesis. *J. Nucl. Med.* **49**, 113S–128S (2008).
- Liu, Y. *et al.* Hybrid BaYbF₅ nanoparticles: novel binary contrast agent for high resolution *in vivo* X-ray computed tomography angiography. *Adv. Health. Mat.* **1**, 461–466 (2012).
- Wang, D. *et al.* Aggregation-enhanced fluorescence in PEGylated phospholipid nanomicelles for *in vivo* imaging. *Biomaterials* **32**, 5880–5888 (2011).
- <http://physics.nist.gov/PhysRefData/XrayMassCoef> [Accessed 20 July 2012].
- Xiong, L. *et al.* High contrast upconversion luminescence targeted imaging *in vivo* using peptide-labeled nanophosphors. *Anal. Chem.* **81**, 8687–8694 (2009).
- Kim, Y. H. *et al.* Tumor targeting and imaging using cyclic RGD-PEGylated gold nanoparticle probes with directly conjugated iodine-125. *Small* **7**, 2052–2060 (2011).
- Kiessling, F. *et al.* RGD-labeled USPIO inhibits adhesion and endocytotic activity of $\alpha_v\beta_3$ -integrin-expressing glioma cells and only accumulates in the vascular tumor compartment. *Radiology* **253**, 462–469 (2009).
- Dubey, P. K., Singodia, D., Verma, R. K. & Vyas, S. P. RGD modified albumin nanospheres for tumour vasculature targeting. *J. Pharm. Pharmacol.* **63**, 33–40 (2011).
- Xiong, L., Yang, T., Yang, Y., Xu, C. & Li, F. Long-term *in vivo* biodistribution imaging and toxicity of polyacrylic acid-coated upconversion nanophosphors. *Biomaterials* **31**, 7078–7085 (2010).
- Cheng, L., Yang, K., Shao, M. W., Lu, X. H. & Liu, Z. *In vivo* pharmacokinetics, long-term biodistribution and toxicology study of functionalized upconversion nanoparticles in mice. *Nanomedicine-Uk* **6**, 1327–1340 (2011).
- Chen, Y. *et al.* Multifunctional mesoporous composite nanocapsules for highly efficient MRI-guided high-intensity focused ultrasound cancer surgery. *Angew. Chem. Int. Ed.* **50**, 12505–12509 (2011).
- Terreno, E., Uggeri, F. & Aime, S. Image guided therapy: the advent of theranostic agents. *J. Control. Release* **161**, 328–337 (2012).
- Koo, H. *et al.* *In vivo* targeted delivery of nanoparticles for theranosis. *Accounts Chem. Res.* **44**, 1018–1028 (2011).
- Hak, S. *et al.* The effect of nanoparticle polyethylene glycol surface density on ligand directed tumor targeting studied *in vivo* by dual modality imaging. *ACS Nano* **6**, 5648–5658 (2012).
- Wang, X., Zhuang, J., Peng, Q. & Li, Y. A general strategy for nanocrystal synthesis. *Nature* **437**, 121–124 (2005).
- Chen, F. *et al.* A "neck-formation" strategy for an anti-quenching magnetic/upconversion fluorescent bimodal cancer probe. *Chem. Eur. J.* **16**, 11254–11260 (2010).
- Li, L. *et al.* Biomimetic surface engineering of lanthanide-doped upconversion nanoparticles as versatile bioprobes. *Angew. Chem. Int. Ed.* **51**, 6121–6125 (2012).
- Peter, M. F., Derek, C. K., Mark, D. D. & John, C. G. Polymer gels for magnetic resonance imaging of radiation dose distributions at normal room atmosphere. *Phys. Med. Biol.* **46**, 3105–3113 (2001).

Acknowledgements

This work has been financially supported by the National Natural Science Foundation of China (Grant No. 50823007, 50972154, 51132009, 51072212, 21172043, 51102259), the



Shanghai Rising Star Program (Grant No. 12QH1402500), the Nano special program of the Science and Technology Commission of Shanghai (Grant No. 11nm0505000, 124119a0400), the Development Foundation for Talents of Shanghai (Grant No. 2012035), the National Basic Research Program of China (973 Program, Grant No.2011CB707905), the China National Funds for Distinguished Young Scientists (51225202) and the Young Investigator Fund of Fudan University (Grant No. EYF163006). We thank Prof. Fuyou Li, Dr. Yang Yang from Fudan University for the help in UCL *in vivo* imaging. We thank Jianan Liu, Feng Chen, Yu Chen, Yan Zhu, Lijun Wang, Jingwei Feng, Linlin Zhang and YanYang from Shanghai Institute of Ceramics, Chinese Academy of Sciences for useful discussions.

Author contributions

H.X., X.Z., W.B. and J.S. conceived the idea and designed the research. H.X., Q.X. and C.W. synthesized the nanocubes and the MAGIC gels, carried the cellular experiments. Q.R. and Y.H. conducted all of the CT tests and analyzed the data. X.Z. and W.G. conducted the radiotherapy experiments and analyzed the data. H.X., S.Z., L.Z., W.P. and K.Z. carried all the animal experiments. H.Q. and Z.W. conducted the ICP-AES tests. All the authors participated in the preparation of the manuscript. W.B. and J.S. supervised the project.

H.X., X.Z., W.B. and J.S. wrote the main manuscript text. H.X., Q.X., C.W., H.Q. and Z.W. prepared figures 1 and 2; H.X., X.Z., Q.R., W.G., Y.H., S.Z., L.Z., W.P. and K.Z. prepared figures 3 and 4. All authors reviewed the manuscript.

Additional information

Supplementary information accompanies this paper at <http://www.nature.com/scientificreports>

Competing financial interests: The authors declare no competing financial interests.

License: This work is licensed under a Creative Commons Attribution-NonCommercial-NoDerivs 3.0 Unported License. To view a copy of this license, visit <http://creativecommons.org/licenses/by-nc-nd/3.0/>

How to cite this article: Xing, H.Y. *et al.* Computed tomography imaging-guided radiotherapy by targeting upconversion nanocubes with significant imaging and radiosensitization enhancements. *Sci. Rep.* 3, 1751; DOI:10.1038/srep01751 (2013).